Adjoint-Based Optimization of a Hypersonic Inlet

Heather Kline[*]

Stanford University, Stanford, CA 94305, U.S.A.

Francisco Palacios[†]

The Boeing Company, Long Beach, CA 90808, U.S.A.

Thomas D. Economon[‡] and Juan J. Alonso[§]

Stanford University, Stanford, CA 94305, U.S.A.

Supersonic combustion ramjets, or scramjets, have the potential to facilitate more efficient transatmospheric flight and airplane-like operations of launch vehicles. A scramjet is an airbreathing engine which uses the compression of air over the forebody and inlet to achieve the conditions necessary for supersonic combustion, using no mechanical compressor. The highly complex flow experienced by three-dimensional hypersonic inlets, demanding performance requirements, and engine design strongly coupled to the vehicle create a need for simulation-based design. Therefore, efficient high-fidelity computation of gradients is desired. In this paper, the derivation, verification, and application of an adjoint formulation for an objective relevant to thrust ($\dot{m}$) will be presented. The design problem addressed is the optimization of a simple hypersonic inlet geometry, however this method is applicable to other engineering problems.

Student Paper Competition Entry.

Nomenclature

Variable Definition

$\vec{A}^c$	convective jacobian
$\vec{A}^v$	viscous jacobian
F	flux vector
J	objective function
$\mathfrak{J}$	lagrangian
U	vector of conservative variables
V	vector of primitive variables
Ψ	vector of adjoint variables
M	transformation matrix between conservative and primitive flow variables
L	matrix of left eigenvectors of the Jacobian
g	generic function
Λ	diagonal matrix of Jacobian eigenvalues
Ω	fluid volume domain
Γ_e	outlet boundary of the fluid domain
Γ_i	inlet boundary of the fluid domain
S	solid wall boundary
$\vec{t}$	unit tangent vector
$\vec{n}$	unit normal vector

[*]Ph.D. Candidate, Department of Aeronautics & Astronautics, AIAA Student Member.
[†]Engineer, Advanced Concepts Group, AIAA Senior Member.
[‡]Postdoctoral Scholar, Department of Aeronautics & Astronautics, AIAA Senior Member.
[§]Professor, Department of Aeronautics & Astronautics, AIAA Associate Fellow.

American Institute of Aeronautics and Astronautics

x, y, z	cartesian coordinates
$\vec{v}$	velocity vector
u, v, w	cartesian components of velocity
E	total energy
H	total enthalpy
M_0	freestream Mach number
c	speed of sound
α	normal boundary deformation
ρ	density
P	static pressure
T	temperature
γ	ratio of specific heats
f	fuel:air ratio

Subscripts

0	freestream
2	entrance to isolator, end of inlet
3	end of isolator, entrance to combustor
4	exit of combustor
10	end of nozzle/ expansion ramp
b	burner
t	total, or stagnation state

Mathematical symbols

∇	nabla, gradient operator
∇_{tg}	tangent derivative on a surface
∂	partial derivative
∂_n	normal derivative to a curve
∂_{tg}	tangent derivative to a curve
∂_x	$\partial/\partial x$
δ	first variation

Units

Pa	Pascals
m	meters
s	seconds

I. Introduction and Motivation

SUPERSONIC combustion ramjets, or scramjets, have the potential to facilitate more efficient transatmo-spheric flight and airplane-like operations of launch vehicles. A scramjet is an airbreathing engine which uses the compression of air over the forebody and inlet to achieve the conditions necessary for supersonic combustion, using no mechanical compressor. These engines operate in hypersonic conditions, ranging from Mach 5 to Mach 10 at current levels of technology. Ramjets have flown up through Mach 5.5, and at Mach numbers of around that magnitude it becomes more efficient to use supersonic combustion.[1] Recent flight tests of the HIFiRE, X-51 and X-43A have had success in achieving positive thrust, while also highlighting the difficulties of designing hypersonic airbreathing engines.[1–3] The highly complex flow experienced by three-dimensional hypersonic inlets, demanding performance requirements, and engine design strongly coupled to the vehicle create a need for simulation-based design. Therefore, efficient high-fidelity computation of gradients is desired. In this paper, the derivation, verification, and application of an adjoint formulation for an objective relevant to thrust ($\dot{m}$) will be presented. The design problem addressed is the optimization of a simple hypersonic inlet geometry, however this method is applicable to other engineering problems.

There is ample existing work in the design of inviscid inlets. The simplest design is a two-dimensional sin-

American Institute of Aeronautics and Astronautics

gle ramp which forms two shocks- the first extending from the nose of the vehicle and meeting the cowl, and the other returning the flow to the horizontal direction. More efficient is the Busemann diffuser[4] which uses a surface designed to result in the Mach waves meeting at a single point, and forming a conical shock which returns the flow to horizontal, as illustrated in Figure 1. This design achieves much of the compression isentropically, resulting in lower stagnation pressure losses. Building off of the Busemann flowfield, streamtracing techniques[5] allow more complex geometries, for example transitioning from a rectangular cross-section at the entrance to a circular cross-section at the combustor to gain benefits from simpler vehicle integration and lower weight combustors. Rectangular-to-Elliptical-Shape-Transition (REST) inlets with boundary layer corrections further build on these concepts.[6] However, even a REST inlet with boundary layer corrections may not achieve the designed performance,[7] due to the complex interactions of shocks and boundary layers in a complex internal hypersonic flow.
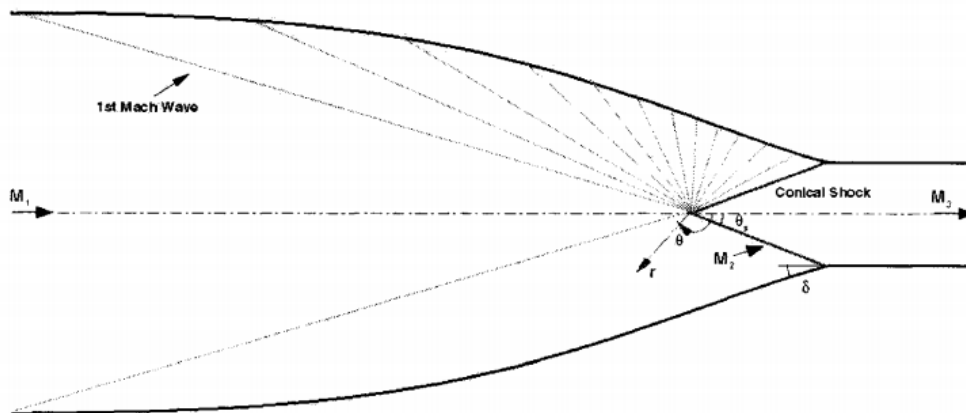

Figure 1: Flowfield of a full Busemann diffuser. Image reproduced from [8].

Modern simulation techniques allow for more efficient high fidelity optimization. Advances in computer speed and efficiency make it possible to complete more function evaluations than previous, however the cpu time required for high-fidelity optimization with large number of design variables is still significant. More efficient calculation of the gradient of the objective function(s) can significantly reduce the time required for optimization. The adjoint method introduced by Jameson[9] provides a more efficient method of calculating gradients, which is independent of the step size and of the number of design variables. An adjoint solution uses information from the direct, or flow solution, to solve a new partial differential equation system which produces analytical gradients to infinitesimal deformations of the surface. The gradients with respect to changes in freestream conditions can be found from the same adjoint solution. Adjoints have been applied to scramjet designs in the past, specifically Wang[10] et al. used a discrete adjoint for a pressure-based functional on the solid surface of a scramjet inlet to accelerate Monte-Carlo characterization of the probability of unstart.

The contributions of this paper are the implementation of a continuous adjoint for the off-body objective function that is the mass flow rate through the outlet, verification by comparison to finite difference, and optimization of simple geometry in inviscid and viscous flows. This builds on previous work by the authors,[11] which used finite difference methods to evaluate the change in performance for a thermoelasticaly deformed inlet, for an objective function of interest to a similar design problem. This paper will begin with a description of the physical problem and generic scramjet geometry followed by the methods used in this work, including the derivation of the adjoint for a mass flow rate objective function will be summarized. The results of verification and optimization cases using this objective function will be shown.

American Institute of Aeronautics and Astronautics

II.   Description of the Physical Problem

Hypersonic Airbreathing Engines

Hypersonic flow begins in the neighborhood of Mach 5, and is defined not with a specified Mach number but as the flight regime where a number of physical phenomena become more significant. These phenomena include thin shock layers where the shock lies very close to the surface of the vehicle, thick boundary layers which interact with the shocks and a large entropy gradient, and the possibility of chemically reacting flow and real gas effects.[12] In terms of the effect on vehicle design, around Mach 5 the cost of decelerating air to subsonic speeds begins to outweigh the cost of supersonic combustion. Combustion at supersonic speeds is more difficult to implement, and issues with residence time, sufficient mixing, and unstart become more significant. The inlets of scramjets need to compress the air sufficiently, while maintaining low drag and high efficiency. Under extreme pressure and heat, there is a higher degree of shape uncertainty. Hypersonic vehicles for access to space are required to operate under a very large range of flight conditions, accelerating to an altitude where rocket propulsion takes over. A diagram of a scramjet is shown in Figure 2. This figure also identifies the stations 0-10 which will be used as subscripts to describe the state of the flow at those locations. Several numbers are left out of this figure for consistency with describing other engines, where there would be more components between the exit of the combustion chamber or burner and the nozzle.
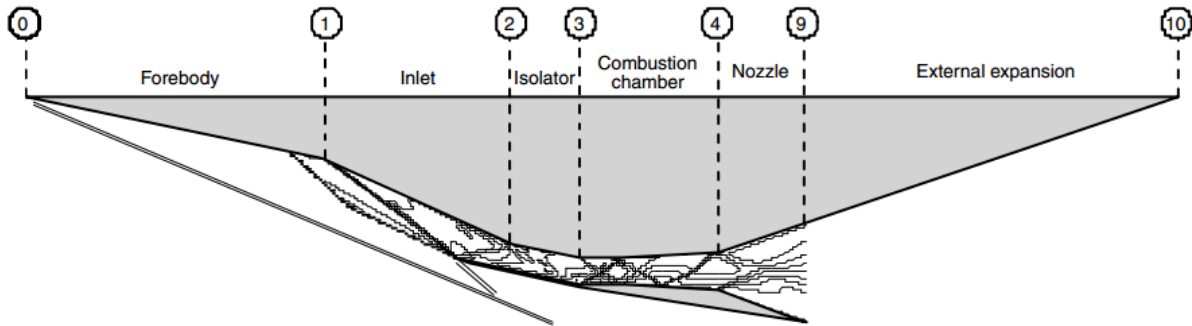

Figure 2: Scramjet flow path. Reproduced from Figure 1 of [13]

Several quantities of interest could be used for optimization. The choice of objective function will strongly determine the outcome. For inlet optimization, the stagnation pressure is often maximized, and there are several other options related to scramjet performance such as the kinetic energy efficiency as described by Smart.[13] In this work, we will be optimizing the mass flow rate, which is directly related to the thrust of the engine. The equation for thrust is shown in Equation 1 and is based on the momentum flux of the air passing through the engine. The derivation of this equation can be found in [14]. The quantities with subscript 0 are the freestream values, and the quantities with subscript 10 are values at the exit of the expansion ramp, as shown in Figure 2. In this equations M is the Mach number, P is the static pressure, T is the temperature, f is the mass flow fraction of fuel:air, c indicates the speed of sound, $\dot{m}$ is the mass flow rate, and subscripts indicate the location along the flowpath as shown in Figure 2.

$$F_x = \dot{m}_0 c_0 M_0 \left((1+f) \frac{M_{10}}{M_0} \sqrt{\frac{T_{10}}{T_0}} - 1 \right) + \frac{A_{10}}{A_0} \left(\frac{P_{10}}{P_0} - 1 \right) \tag{1}$$

For the purposes of this work, we would like to optimize this inlet without needing to calculate the values through the combustor. While the values at station 10 will be dependent on several other quantities which could be calculated on the inlet, the mass flow rate is an intuitive and simple quantity to use in this case. In Section III, we will see that this choice of objective function results in a very simple formulation.

Model Case

The flight conditions chosen are Mach 7.0 with a freestream temperature of $221.9 \deg K$, and freestream static pressure of $2183.37 Pa$. These conditions correspond to conditions used in previous work[11] for verification. The resulting Reynolds number for an inlet of 1.0 meter is about 5×10^6. These conditions correspond

American Institute of Aeronautics and Astronautics

to $75kPa$ at Mach 7. Undersped cases have a Mach number of 5.0 and the same freestream pressure and temperature.

A simple two-dimensional geometry used to verify adjoint results and as an initial point for optimization. This geometry was designed using oblique shock equations[15] such that the shock resulting from the angle of the ramp meets the cowl lip. The height of the isolator and length of the cowl are designed such that the second shock impinges at the end of the ramp, leading to horizontal flow at the isolator. The parameters of this design are a desired static pressure ratio of 20.0, a design Mach number of 7.0, and an inlet length of 1.0 meters. A schematic and dimensions are also included in the appendix. The geometry is shown in Figure 3. The nose and cowl have been filleted to have a radius of 0.0005 meters in order to avoid sharp edges.
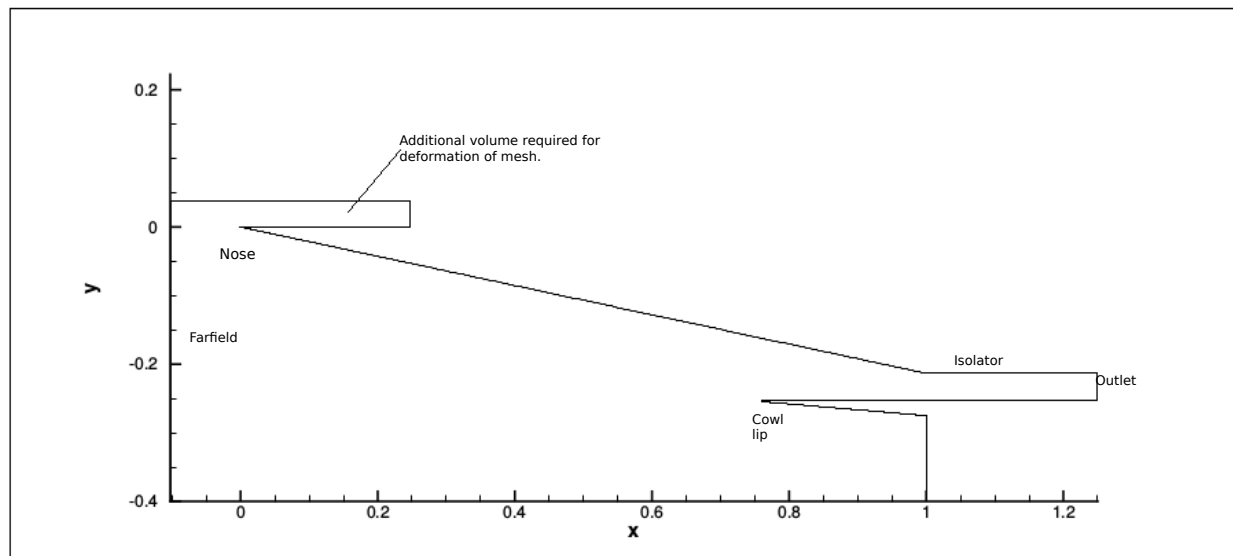
Figure 3: Baseline geometry used as initial point in optimization and for verification of adjoint method.

At Mach 7 in inviscid flow, this design is expected to be a local maximum for mass flow rate, if the height between the nose and cowl remains constant. Due to the supersonic nature of the flow if the leading shock (starting at the cowl lip) moves further downstream towards the isolator the mass flow rate should remain constant. If that shock is moved upstream from the cowl the flow will spill out around the cowl, reducing the mass flow rate. When viscous effects are included or when at off-design conditions this shape will not be an optimum. At off-design conditions of a lower Mach number the mass flow rate can be increased by moving the shock closer to the cowl lip. The straight ramp design is chosen as the initial point rather than a Busemann flow field for its simplicity.

For three-dimensional simulations the two-dimensional geometry is extruded to have a width of 0.1 meters. This geometry is simulated as symmetric about the center of the inlet, and the actual geometry simulated has a width of 0.05 meters. Side walls are added to complete this geometry, connecting the nose to the cowl. Once again, the edges of this geometry have been rounded with a radius of 0.0005 meters to avoid sharp edges in the simulation, which can cause convergence issues[16] as well as increasing the likelihood of overlapping geometry when deformations are applied. This geometry is illustrated in Figure 4.

III.   Adjoint Derivation With An Off-Body Objective Function

A continuous adjoint problem, using information from the direct, or flow solution, solves a new partial differential equation system which produces analytical gradients to infinitesimal deformations of the surface. These sensitivities can be projected into any arbitrary deformation. The gradients with respect to changes in freestream conditions can be found from the same adjoint solution. This method requires a second PDE system and the derivation of boundary conditions that depend on the objective function of interest. While a new set of boundary conditions is required for every new objective function, this method provides gradients for an arbitrary number of design variables for approximately the same computational cost as a single additional direct solution. By comparison, the finite difference method of calculating gradients
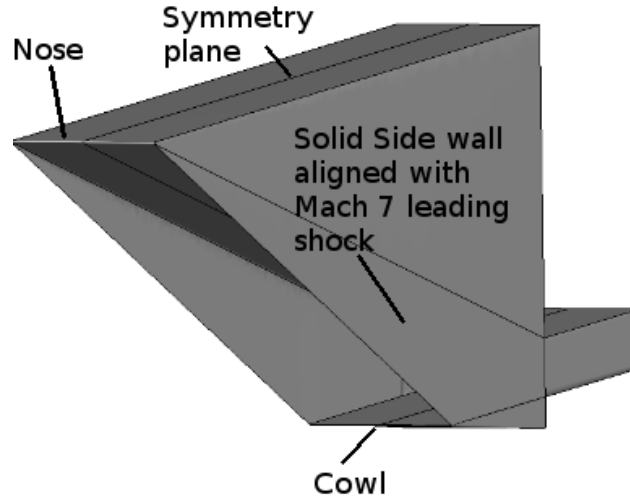
Figure 4: Three-dimensional baseline geometry.

requires an additional direct solution for every additional design variable. A great deal of literature exists on adjoints and their derivation. The method was introduced by Jameson,[9] and further work by Giles & Pierce,[17] Castro[18] et al., Hayashi[19] et al., and Economon[20] provide additional details for the derivation and solution of adjoints. This work adds the derivation for the boundary conditions for the off-body functional $\dot{m}$. The outlet objective function for total pressure has been developed previously by Papadimitriou & Giannakoglou,[21] using a similar process.

When an adjoint is derived for an objective function, J, defined on some surface other than a solid body, it is called an off-body functional - for example, the mass flow rate $\dot{m}$ defined on the exit plane of an inlet. In these equations, U refers to the vector of conservative variables, F is the vector of fluxes, A^c is the convective jacobian, V is the vector of primitive variables, and M is the transformation matrix between the conservative and primitive variables. W is the vector of characteristic variables, which are constant along characteristics of these equations. Ψ is the vector of adjoint variables. The adjoint variables, $\Psi = (\psi_\rho, \psi_{\vec{\rho v}}^T, \psi_{\rho E})^T$ are Lagrange operators for the direct system of equations, in this case the Euler Equations. Ω represents the volume.

Let us assume the objective function is defined as an integral over an outlet surface Γ_e. Equation 2 shows this integral for the objective function of $\dot{m}$. For generality the term g will be used for intermediate steps of the derivation, and expanded when necessary.

$$J = \int_{\Gamma_e} g ds = \int_{\Gamma_e} \rho \vec{v} \cdot \vec{n} ds \tag{2}$$

Our goal is to find $\frac{\partial J}{\partial S}$, where S is the surface to be designed. In order to find this value, we set up a variational problem under the constraint that the variations of the flow variables must satisfy the direction problem. This constraint is satisfied by setting the variation of the residual $\mathcal{R}(U)$ to zero. $\mathcal{R}(U)$ is expanded for the steady Euler Equations in Equations 3-4.

$$\mathcal{R}(U) = \nabla \cdot \vec{F} = \frac{\partial}{\partial t}(U) + \nabla \cdot \vec{A} U$$
$$\delta \mathcal{R}(U) = \nabla \cdot \vec{A} \delta U \tag{3}$$

The Jacobian A^c is expanded in the appendix. The conservative variables U and primitive variables V are defined as:

American Institute of Aeronautics and Astronautics

$$U = \left\{ \begin{array}{c} \rho \\ \rho\vec{v} \\ \rho E \end{array} \right\} , V = \left\{ \begin{array}{c} \rho \\ \vec{v} \\ P \end{array} \right\}. \tag{4}$$

The Lagrangian is defined in Equation 5, where the adjoint variables Ψ are introduced as the Lagrange multipliers in the application of the constraint.

$$\mathcal{J} = J - \int_\Omega \Psi^T \mathcal{R}(u) d\Omega$$

$$\delta\mathcal{J} = \delta J - \int_\Omega \Psi^T \delta\mathcal{R}(U) d\Omega \tag{5}$$

In order to solve this problem for the sensitivity $\frac{\partial\mathcal{J}}{\partial S}$, which will be equated to $\frac{\delta\mathcal{J}}{\delta S}$, we need to eliminate dependence on δU. This is accomplished first through linearizing the governing equations and applying known relationships between variables from the direct problem, and then through applying boundary conditions that eliminate the remaining undesired variational terms. The linearization of the governing equations and their boundary conditions is shown in Equation 6. The variation of characteristic variables along the positive characteristics is zero, the velocity is tangent to the wall, and the variation of the residual is zero.

$$\left\{ \begin{array}{lll} \delta\mathcal{R} = \nabla \cdot \vec{A}\delta U & = 0 & \text{in } \Omega \\ \delta\vec{v} = -\partial_n(\vec{v})\,\delta S & & \text{on } S \\ (\delta W)_+ & = 0 & \text{on } \Gamma_\infty \end{array} \right. \tag{6}$$

The variation of J is expanded in Equation 7. It is reasonable to assume for this problem that the outlet surface will be undeformed, such that the term $\delta\Gamma_e$ can be set to 0. For functional defined on the solid body being designed, these terms cannot be set to 0.

$$\delta J = \int_{\delta\Gamma_e} g(U) ds + \int_{\Gamma_e} \frac{\partial g}{\partial U}\delta U ds$$

$$\int_{\delta\Gamma_e} g(U) ds = \int_{\Gamma_e} \frac{\partial g(U)}{\partial U}(\delta S \cdot \nabla U) ds + \int_{\Gamma_e} g(U)\delta ds = 0 \tag{7}$$

$$\delta J = \int_{\Gamma_e} \frac{\partial g}{\partial U}\delta U ds = \int_{\Gamma_e} \frac{\partial g}{\partial V}\delta V ds$$

Applying the Divergence Theorem, the expression for $\delta\mathcal{J}$ in Equation 5 can be rewritten as shown in Equation 8. In these equations Γ refers to the open boundary (farfield, inlet, and exit boundaries), S refers to the solid surface, and Γ_e refers to the boundary over which $\dot{m}$ is calculated. Γ_e overlaps with Γ.

$$\delta\mathcal{J} = \delta J - \int_\Omega \Psi^T \delta\mathcal{R}(U) d\Omega$$

$$\int_\Omega \Psi^T \delta\mathcal{R}(U) d\Omega = \int_\Gamma \Psi^T \vec{A}\cdot\vec{n}\delta U ds + \int_S \Psi^T \vec{A}\cdot\vec{n}\delta U ds + \int_S \Psi^T \vec{A}\cdot\vec{n}\delta S ds - \int_\Omega \nabla\Psi^T \vec{A}\delta U d\Omega \tag{8}$$

$$\delta\mathcal{J} = \int_{\Gamma_e} \frac{\partial g}{\partial U}\delta U ds - \int_\Gamma \Psi^T \vec{A}\cdot\vec{n}\delta U ds - \int_S \Psi^T \vec{A}\cdot\vec{n}\delta U ds - \int_S \Psi^T \vec{A}\cdot\vec{n}U\delta S ds + \int_\Omega \nabla\Psi^T \vec{A}\delta U d\Omega$$

We can now express the adjoint problem as shown in Equation 9, where the integral over the volume from Equation 8 defines the PDE to solve, and the integrals over the boundaries of the domain (Γ, S) provide the boundary conditions. A shorthand term is introduced for the momentum components of the adjoint variables, $\vec{\varphi} = \{\psi_{\rho u}, \psi_{\rho v}, \psi_{\rho w}\}^T$. For convenience, the primitive variables V will now be used.

$$\left\{ \begin{array}{lll} -\nabla\Psi^T \cdot \vec{A} & = 0 & \text{in } \Omega \\ \frac{\partial g}{\partial V}\delta V - \Psi^T \vec{A}\cdot\vec{n}M\delta V & = 0 & \text{on exit surface } \Gamma_e \\ \Psi^T \vec{A}\cdot\vec{n}M\delta V & = 0 & \text{on open boundaries } \Gamma \neq \Gamma_e \\ \vec{\varphi} = -\psi_{\rho E}\vec{v} & & \text{on solid walls } S \end{array} \right. \tag{9}$$

American Institute of Aeronautics and Astronautics

The terms at the outlet are expanded for the mass flow rate objective function in Equation 10. The term $v_n = \vec{v} \cdot \vec{n}$.

$$\frac{\partial g}{\partial V}\delta V - \Psi^T \vec{A} \cdot \vec{n} M \delta V = 0$$

$$v_n \delta\rho + \rho\vec{n} \cdot \delta\vec{v} - \left\{ \begin{array}{c} \psi_\rho v_n + \vec{v} \cdot \vec{\varphi} v_n + \psi_{\rho E} v_n \left(\frac{\vec{v}^2}{2}\right) \\ \rho(\vec{v} \cdot \vec{\varphi})\vec{n} + \rho v_n \vec{\varphi} + \rho\psi_\rho \vec{n} + \psi_{\rho E}(\rho v_n \vec{v} + \rho(\frac{c^2}{\gamma-1} + \gamma\frac{\vec{v}^2}{2})\vec{n}) \\ \vec{\varphi} \cdot \vec{n} + \psi_{\rho E}(v_n \frac{\gamma}{\gamma-1}) \end{array} \right\}^T \left\{ \begin{array}{c} \delta\rho \\ \delta\vec{v} \\ \delta P \end{array} \right\} = 0 \quad (10)$$

Under subsonic conditions, the pressure at the outlet is specified and therefore $\delta P = 0$. Eliminating the dependence on the remaining, arbitrary, variations leads to Equation System 11.

$$v_n - \left(\psi_\rho v_n + \vec{v} \cdot \vec{\varphi} v_n + \psi_{\rho E} v_n \left(\frac{\vec{v}^2}{2}\right)\right) = 0$$

$$\rho\vec{n} - \left(\vec{n}\left(\rho(\vec{v} \cdot \vec{\varphi}) + \rho\psi_\rho + \psi_{\rho E}\rho\left(\frac{c^2}{\gamma-1} + \gamma\frac{\vec{v}^2}{2}\right)\right) + \vec{\varphi}(\rho v_n) + \vec{v}(\psi_{\rho E}\rho v_n)\right) = \vec{0} \quad (11)$$

The boundary condition at the outlet in terms of the energy adjoint variable reduces to Equation 12. When the exit experiences supersonic flow, δP becomes arbitrary, introducing an additional equation which is satisfied when $\psi_{\rho E} = 0$. This reduces the boundary condition to Equation 13. Equations 12 and 13 are the critical result of this derivation, and of this work. Applying this boundary condition, along with the conditions at boundaries not included in the objective function, result in the ability to find the variation of $\dot{m}$ with respect to the normal variation of the surface δS. The correctness of the assumptions made in the derivation of these equations, and their implementation, will be tested in the verification section of this work.

$$\left\{ \begin{array}{c} \psi_\rho \\ \vec{\varphi} \\ \psi_{\rho E} \end{array} \right\}_{\Gamma_e, M_e < 1} = \left\{ \begin{array}{c} \psi_{\rho E}\left(\frac{c^2}{\gamma-1} + \frac{|\vec{v}|^2}{2}\right) + 1 \\ \psi_{\rho E}\left(\frac{-c^2}{\vec{v}\cdot\vec{n}(\gamma-1)}\vec{n} - \vec{v}\right) \\ \psi_{\rho E} \end{array} \right\} \quad (12)$$

$$\left\{ \begin{array}{c} \psi_\rho \\ \vec{\varphi} \\ \psi_{\rho E} \end{array} \right\}_{\Gamma_e, M_e > 1} = \left\{ \begin{array}{c} 1 \\ \vec{0} \\ 0 \end{array} \right\} \quad (13)$$

For the viscous case Equation 14 could be applied to account for perturbations of the eddy viscosity, however it will be neglected for this work. This simplification is also assumed at farfield boundaries, and is the convention for continuous adjoints. Viscous terms do appear in the volume integral and at solid boundaries in the adjoint formulation for viscous flow.

$$\psi^T(\vec{A^v})\delta V \cdot \vec{n} + \psi^T\delta \left\{ \begin{array}{c} \cdot \\ \bar{\bar{\sigma}} \\ \bar{\bar{\sigma}} \cdot \vec{v} \end{array} \right\} \cdot \vec{n} + \psi^T\delta \left\{ \begin{array}{c} \cdot \\ \cdot \\ \mu_{tot}^2 c_p \nabla T \end{array} \right\} \cdot \vec{n} + \vec{n} \cdot \left(\Sigma^\varphi + \Sigma^{\psi_{\rho E}\vec{v}}\right) - \frac{\partial g}{\partial V}\delta V = 0 \quad (14)$$

At the inlet to the computational volume, the boundary condition is defined by $\int_{\Gamma_i}(\Psi^T \vec{A} \cdot \vec{n}\delta U)ds = 0$. In supersonic flow, all of the characteristic are exiting, leading to the condition that the adjoint variables are interpolated from the volume solution as the iterative solution progresses. At farfield boundaries we assume that the variations of the conservative variables, δU are negligible, which is consistent with the boundary condition of the direct problem.

After application of the boundary conditions that eliminate the dependence on the variation in the conservative variables δU, and assuming only normal deformations, the remaining terms on the surface in Equation 8 can be reduced to the terms shown in Equation 15, defining the surface sensitivity, $\frac{\partial \mathcal{J}}{\partial S}$, which is multiplied by the normal deformation δS in Equation 15. A full derivation of this term can be found in work by Castro.[18]

American Institute of Aeronautics and Astronautics

$$\delta \mathcal{J} = \int_S \frac{\partial \mathcal{J}}{\partial S} \delta S ds$$

$$\frac{\partial \mathcal{J}}{\partial S} = (\nabla \cdot \vec{v})(\rho\psi_\rho + \rho\vec{v} \cdot \psi_{\rho\vec{v}} + \rho H \psi_{\rho E}) + \vec{v} \cdot \nabla(\rho\psi_\rho + \rho\vec{v} \cdot \psi_{\rho\vec{v}} + \rho H \psi_{\rho E})$$

(15)

The surface sensitivity defined in Equation 15 is defined at every point on the surface assuming a continuous surface and continuous solution to the direct problem. In theory the application of the divergence theorem during the derivation should require that discontinuities like shocks in the flow should be treated differently, e.g., by sensing the shock location and applying an additional boundary condition along that surface. In practice, as shocks are not true discontinuities within the numerical flow solution, this is not necessary and gradients without a shock correction match well with finite difference results. It has also been assumed that viscous perturbations at the outlet, inlet, and farfield boundary conditions are negligible.

This derivation has focused on the inviscid problem. In the viscous problem, the boundary conditions on the surface and the equation for the surface sensitivity are modified. At inlet and outlet boundary conditions the viscous perturbations are assumed negligible, and these boundary conditions to not change. The equations defining these boundary conditions and the viscous surface sensitivity can be found in Reference [22]. Since the viscous perturbations at the outlet are neglected in this work, the boundary conditions developed here remain unchanged.

IV. Numerical Implementation

Computational Fluid Dynamics

The open-source CFD suite SU2, developed in the Aerospace Design Lab at Stanford University,[23] was used to generate flow solutions and the adjoint solution. A new boundary condition and other modifications were implemented in order to produce the continuous adjoint solution for $\dot{m}$. The Euler Equations were used in verification and in initial optimization cases. The Reynolds Averaged Navier Stokes equations with the SA turbulence model was used for viscous simulations.

SU2 uses the Finite Volume Method (FVM) to solve partial differential equations including the Reynolds-Averaged-Navier-Stokes (RANS) equations and the Euler equations. This software suite uses unstructured meshes to discretize the volume. In the RANS equations, a turbulence model is used to account for the Reynolds stresses. The one-equation Spalart-Allmaras and two-equation SST k-omega turbulence models are available. The adjoint equations are solved in a similar fashion, re-using methods implemented to solve partial differential equations and the information generated by the flow solver.

Free-Form Deformation Variables

A Free-Form Deformation (FFD) strategy has also been adopted in both two and three dimensions, which has become a popular geometry parameterization technique for aerodynamic shape design.[24–26] In FFD, an initial box encapsulating the object (rotor blade, wing, fuselage, etc.) to be redesigned is parameterized as a Bézier solid. A set of control points are defined on the surface of the box, the number of which depends on the order of the chosen Bernstein polynomials. The solid box is parameterized by the following expression:

$$X(u,v,w) = \sum_{i,j,k=0}^{l,m,n} P_{i,j,k} B_j^l(u) B_j^m(v) B_k^n(w),$$

(16)

where u, v, $w \in [0, 1]$, and B^i is the Bernstein polynomial of order i. The Cartesian coordinates of the points on the surface of the object are then transformed into parametric coordinates within the Bézier box.

The control points of the box become design variables, as they control the shape of the solid, and thus the shape of the surface grid inside. The box enclosing the geometry is then deformed by modifying its control points, with all the points inside the box inheriting a smooth deformation. Once the deformation has been applied, the new Cartesian coordinates of the object of interest can be recovered by simply evaluating the mapping inherent in Eqn. 16. An example of FFD control point deformation to a wing geometry appears in Fig. 5.[22]

American Institute of Aeronautics and Astronautics
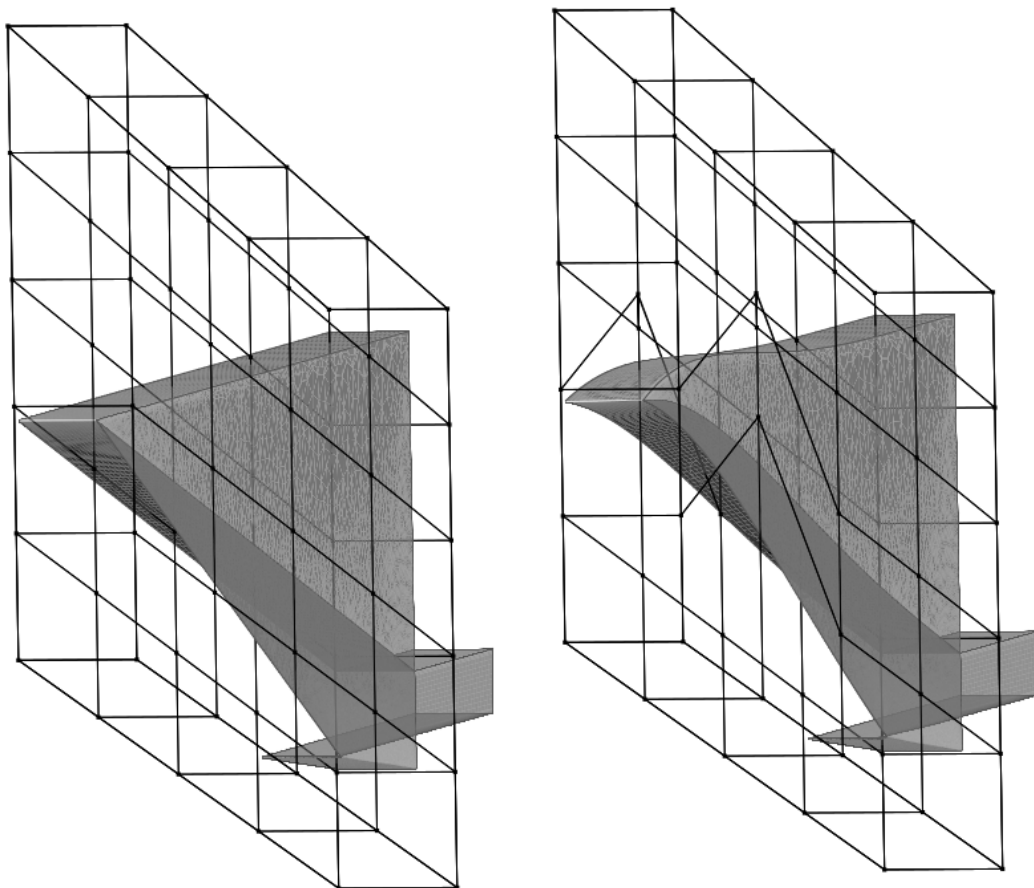
(a) Original wing surface (grey) and FFD bounding box with control points at the intersection of the black lines.

(b) Deformed wing surface after displacement of the FFD control points near the compression ramp.

Figure 5: An example of the FFD technique applied to the three-dimensional inlet geometry.

American Institute of Aeronautics and Astronautics

Optimization Method

The optimization method used in this work is the fmin_slsqp function from the Python[TM] version 2.7.6 module scipy.optimize. This optimization method is a bounded, gradient based optimization using sequential least square programming.[27] The adjoint method was used to provide gradients in these optimization results, and the design variables were constrained by a maximum amplitude of 0.1 meters unless otherwise stated. This optimization problem is expressed in Equation 17. The optimizer is also limited to 10 iterations, to reasonably limit the time required and because in the cases presented here the majority of the design gains were achieved within the first two or three iterations.

V.   Results

As this is both a new boundary condition being applied and implemented, verification is required prior to application of the results to optimization. In the following sections, verification is presented for the gradient values computed by the adjoint method compared to gradients computed by finite difference. Following the verification, the adjoint method was applied to example optimization problems which successfully increased the mass flow rate up to the point where the leading shock meets the cowl.

Adjoint Method Verification

In order to verify that the implementation of the adjoint for mass flow rate operates satisfactorily, in this section we compare the gradients computed with the adjoint method to gradients computed with finite differences. This will include two and three dimensional simulations using the Euler equations, and two dimensional simulations using the RANS equations. These results have been selected to be relevant to the optimization results presented later.

Results for an inviscid case are shown in Figure 7, using the 7 design variables shown in Figure 6. The 0th design variable controls the nose length through a horizontal deflection, while the 1st - 6th design variables control the shape of the ramp through vertical deflections. Figure 6 shows all design variables at a positive 0.01 deflection.
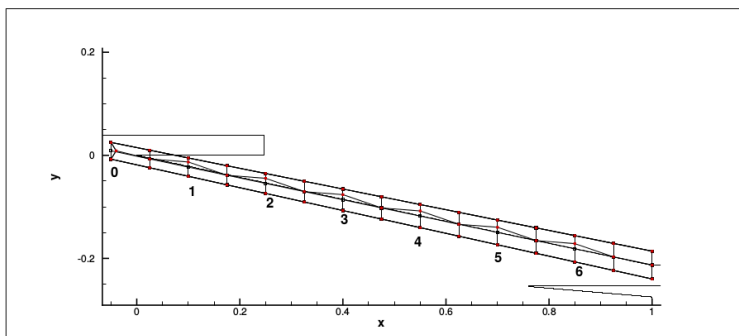

Figure 6: Illustration of numbered design variables for 7-DV cases. Figure overlays FFD box with undeformed (black/unfilled points) and deformed (red/filled points) control points.

Figure 8 shows a similar trend in the gradients computed for the viscous case, at Mach 7. This figure includes the gradients computed by finite difference for inviscid flow for comparison. The gradients are not as closely matched as the inviscid results, however the difference is small enough that these gradients may be used for optimization. The sensitivities are larger for viscous flow, particularly at the design variables in the middle of the ramp. The trend of higher sensitivity for viscous results is consistent with the results of Kline,[11] where a finite difference methodology on a three dimensional geometry indicated greater sensitivity of one-dimensionalized flow quantities in viscous flow as opposed to inviscid flow.

Figure 9 illustrates the effect of using the sharp edge sensitivity removal on the adjoint gradient computation.[16] The sharp edge sensitivity removal filters sensitivites near sharp edges where the adjoint solution is expected to be less accurate, and the distance away from a sharp edge that this filter is applied is controlled by a coefficient. As seen in Figure 9, the sharp edges of the geometry do experience large sensitivities which

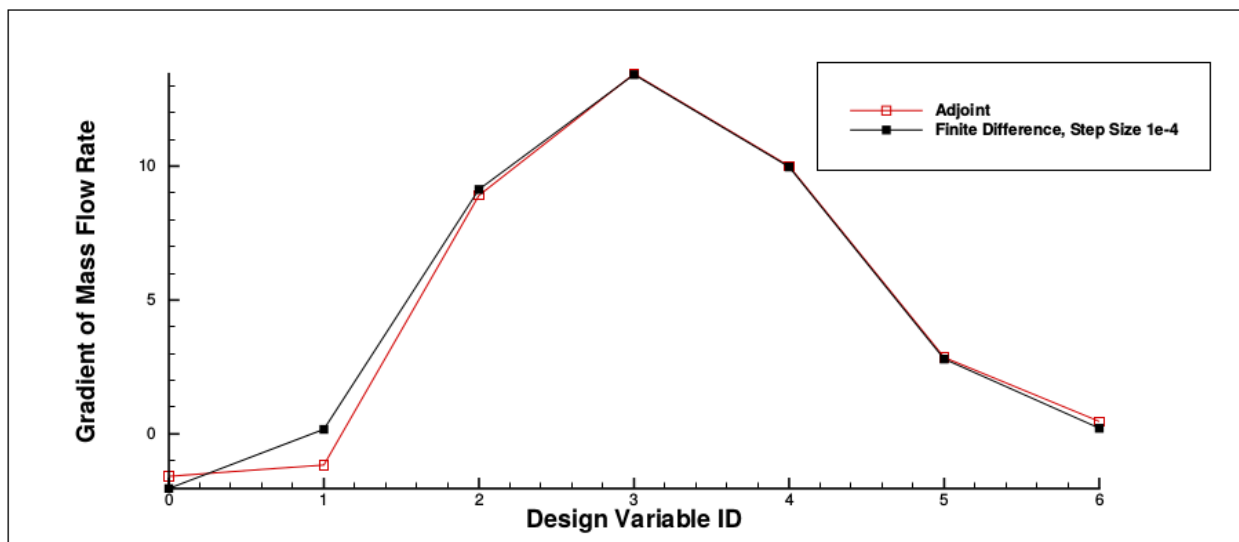American Institute of Aeronautics and Astronautics

Figure 7: Gradient verification for Mach 5.0, inviscid flow, with 7 Design Variables. Design variable definitions are shown in Fig. 6.
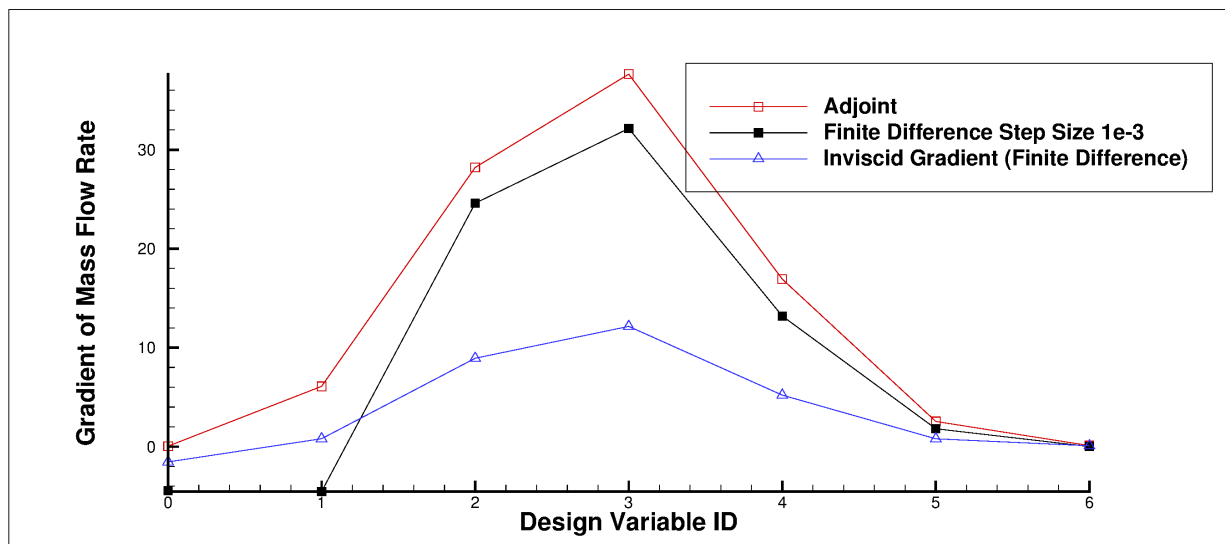

Figure 8: Gradient verification for Mach 7.0, viscous flow, with 7 design variables illustrated in Figure 6. Gradients at Mach 7 for inviscid flow are also included for comparison.

may be inaccurate, however removing too much is also undesirable. Sharp edge sensitivity removal was also used in the three-dimensional inviscid case.

Sharp edge sensitivity removal for the three-dimensional case is shown in Figure 10. This plot also illustrates the sensitvity solution, showing that in addition to high sensitivity near the nose, there are also large values in regions of the side wall and ramp surface. While sharp edge sensitivity removal resulted in closer matching with the finite difference, this also results in an unexpected result of relatively low sensitivity near the nose in both the finite difference and adjoint results.

Figure 12 compares the inviscid gradient values calculated on the three-dimensional geometry shown in Figure 4. In order to achieve these results, the sharp edge sensitivity removal had to be used; without this correction to the adjoint solution the sensitivity at the nose (0th design variable) had an amplitude approximately 6x that of the finite difference result. With or without this correction to the adjoint, the

American Institute of Aeronautics and Astronautics
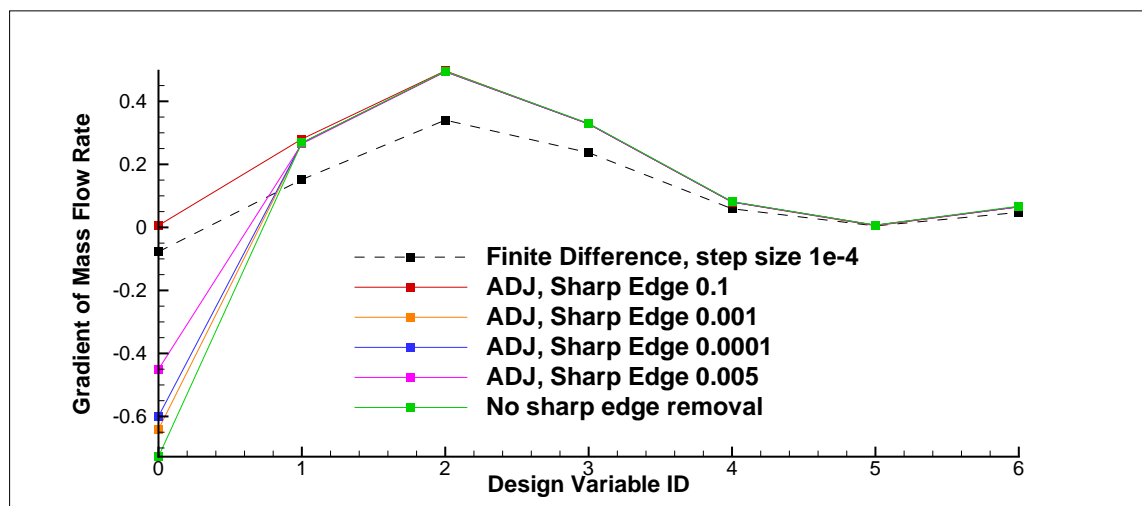
Figure 9: Illustration of sharp edge filter in Mach 5.0 three dimensional inviscid flow. Increasing the coefficient value controls the area around a sharp edge where the filter will be applied.

trend in the gradients is similar, and as such should produce similar results when used for optimization. The design variables used for three-dimensional verification are shown in Figure 11.

Optimization Results

The optimization problem is solved by the optimization method described in Section IV, physical model described in Section IV, and a new adjoint-based gradient described in Section III. The specific optimization problem addressed is described in Equation 17 and in Section II. The mass flow rate $\dot{m}$ is minimized with constrained maximum deformations of the FFD control points $\vec{x}$.

$$\min_{\vec{x}} J(\vec{x}) = -\int_{\Gamma_e} \rho \vec{v} \cdot \vec{n} \, ds = -\dot{m}_e$$
$$\text{subject to: } \vec{x} \leq 0.1$$

(17)

Two-Dimensional Inviscid Optimization Results

The design variable used for the two-dimensional problem are the same as the 7 design variables shown in Figure 6 used to verify the adjoint gradients. Optimizing at the design condition of Mach 7.0 results in a very slight change in geometry, as shown in Fig. 13. The shock has moved from meeting the cowl lip to impinging on the cowl slightly downstream of the cowl lip. The mass flow rate has increased very slightly, by 0.63%, indicating that the initial design had a small amount of spillage over the cowl lip.

As the initial geometry is near-optimal at Mach 7.0 it is interesting to investigate the optimization results at different flight conditions. At higher Mach numbers the shock will move further within the inlet, and
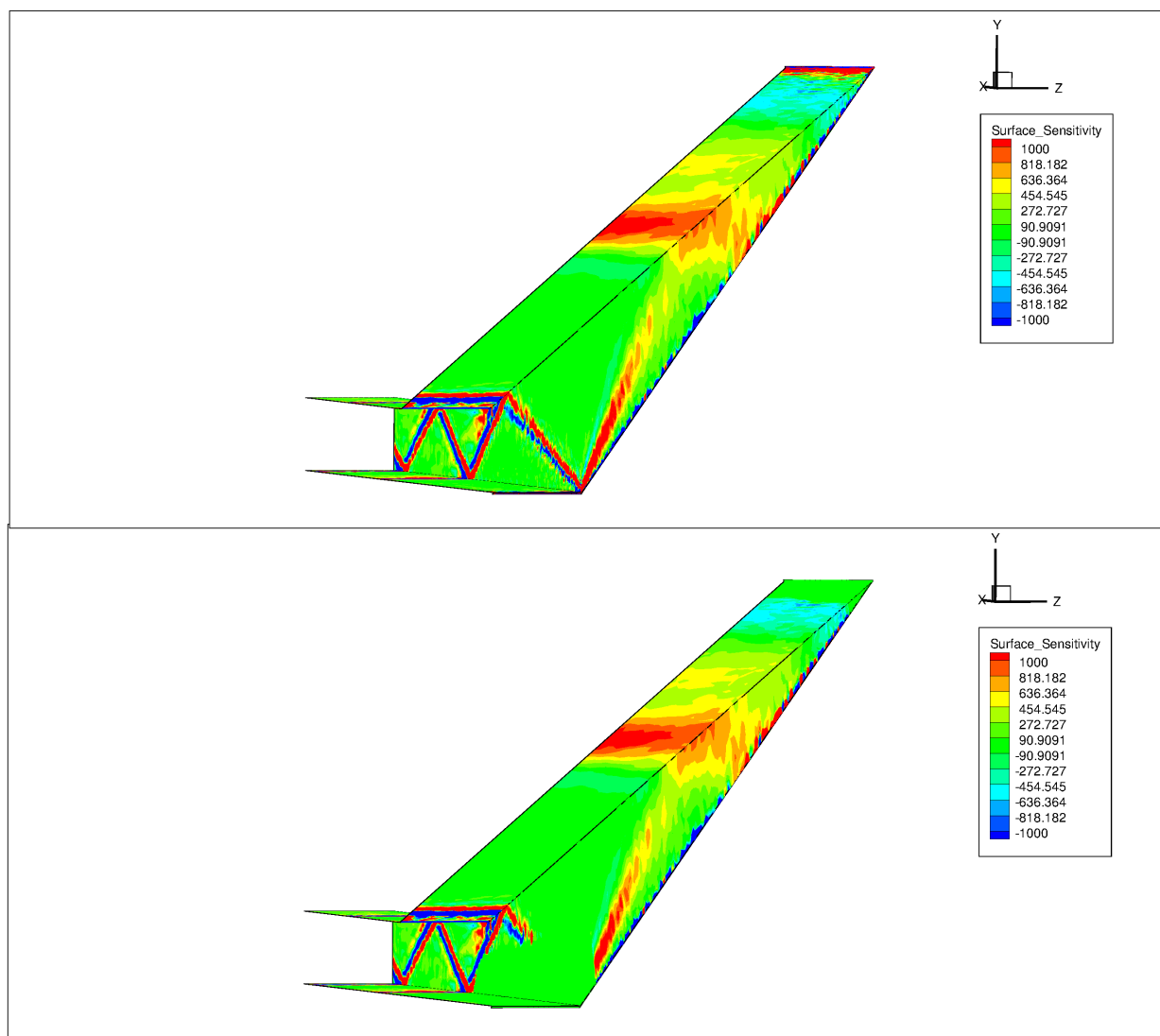
American Institute of Aeronautics and Astronautics

Figure 10: Illustration of surface sensitivity solution. Upper plot shows solution without sharp edge sensitivity removal. Lower plot shows sharp edge sensitivity removal with a coefficient of 0.03, which has resulted in sensitivities of 0 near corner points.

small changes to the geometry will not change the mass flow rate compared to the initial geometry. This was confirmed by optimizing at Mach 8.0 and Mach 9.0. At lower Mach numbers the result is more interesting. The optimization results at Mach 5.0 are shown in Fig. 14.

The optimizer completed due to reaching a maximum number of iterations. Within the first iteration, the mass flow rate increased by 25.75%, and increased by a total of 25.78% over ten iterations of the optimizer. The final shape places the leading shock very near the cowl. Although the contour of the compression ramp after the leading shock is established will not effect the mass flow rate, nevertheless this method has produced a smooth curve which does not produce any additional shocks prior to the shock emanating from the cowl lip.

Three-Dimensional Inviscid Optimization Results

The three-dimensional geometry is discussed in Section II. Optimization results at a freestream Mach number of 5.0 are shown alongside the original geometry in Figure 16. The free-form-deformation box for this case is shown in Figure 15, with a total of 15 design variables consisting of horizontal (x) motion of the nose and

American Institute of Aeronautics and Astronautics
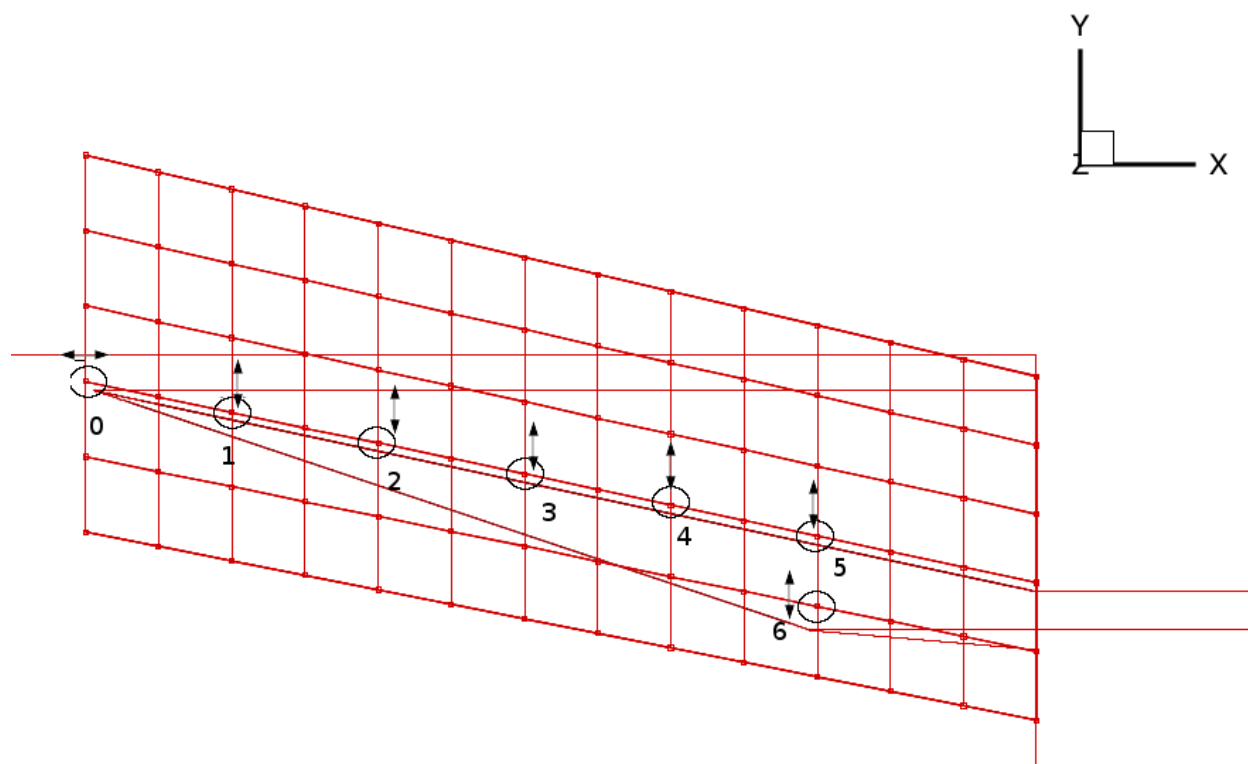
Figure 11: Illustration of Numbered Design Variables for 3-D adjoint verification. Design variables lie in the symmetry plane.

cowl, vertical (y) motion at locations along the ramp and at the cowl, and span-wise (z) deformation of the side wall. In Figure 16, it can be seen that the leading shock around the original geometry extends outwards around the side wall, whereas in the optimized geometry this shock not only meets the cowl at the symmetry plane (as was the case for the two-dimensional optimization), but also meets the edge of the side wall.

The initial and final geometry are overlaid in Figure 17, and the objective history is shown in Figure 18.

2-Dimensional Viscous Optimization Results

The flow field at the baseline design at Mach 7 is shown in Figure 19a. Reynolds-Averaged Navier-Stokes flow with the Spalart-Almaras turbulence model was used. The JST[28] scheme for numerical integration, with a mesh of 1,120,620 elements, illustrated in the appendix. We can see in Figure 19a that in the viscous case at the nominal Mach number to shock is pushed just outside the cowl lip, causing more spillage than occurred for the inviscid case. The isolator has been removed from this simulation.

The optimizer is able to use the gradient information to move the shock such that flow is not deflected below the cowl, resulting in the maximum capture area that can be achieved without changing the height of the inlet. However, this has also resulted in an area of separation on the cowl, as can be seen in Figure 19b - a phenomenon which will reduce the performance of the inlet, and which cannot be captured by the use of $\dot{m}$ by itself. The presence of boundary layers caused the original design to have a 2.9% decrease relative to the inviscid simulation, which was recovered through the optimization.

Although in this case a separation bubble has formed on the cowl, the oversped condition where the leading shock impinges on the cowl surface rather than the cowl leading edge is not unequivocally negative. The mass flow rate is unchanged from the shock-on-cowl condition, and there is increased non-uniformity in the flow entering the combustor. In addition to providing a buffer allowing reasonable operation just below the nominal Mach number, it is suggested by Turner[29] et al. that the resulting shock train provides additional mixing desirable for the performance of the combustor in some designs.
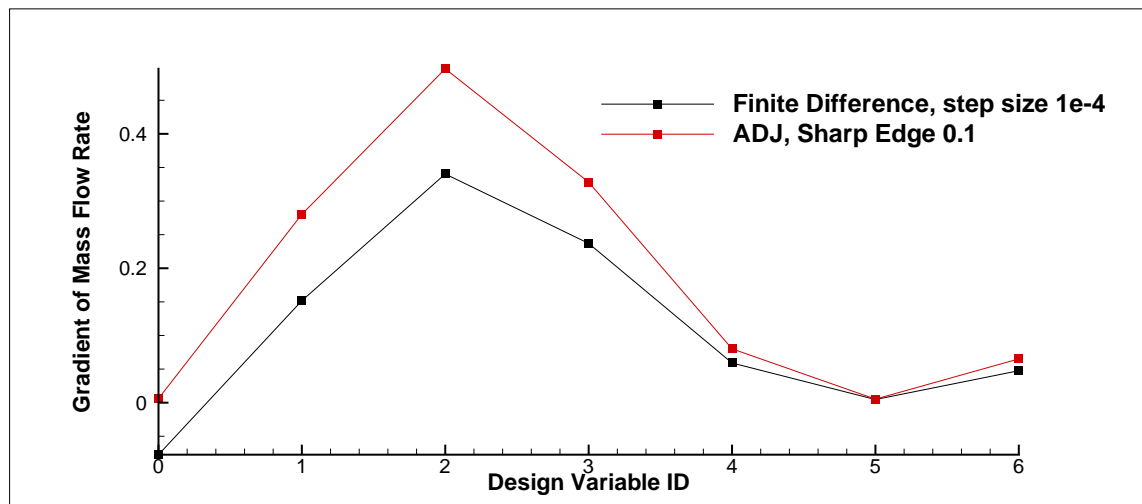
American Institute of Aeronautics and Astronautics

Figure 12: Gradient verification in Mach 7.0, three-dimensional inviscid flow.

VI. Conclusions

The adjoint boundary conditions for $\dot{m}$ integrated over an outlet surface were implemented in SU2, and verified by comparison to finite different results for two- and three-dimensional inviscid flow, as well as for viscous two-dimensional flow. In order to match well with the finite difference, a sharp edge sensitivity removal was applied to the adjoint solution. This was successful in achieving acceptable agreement between the adjoint and finite difference, as well as in achieving reasonable optimization results. Determining whether the sensitivities near the sharp nose of this inlet should be removed, or corrected in another way, or if further accuracy is required for the finite difference, would be interesting topics for future research.

A geometry designed to satisfy a shock-on-cowl condition at Mach 7 was optimized for maximum $\dot{m}$ at Mach 5, resulting in geometries which moved the shock back to the cowl within one or two iterations for both two and three-dimensional geometries. This adds further confidence to the use of the adjoint method to compute the gradients for this objective function. The results of this work are summarized in Table 1. The gradients were of a quality to be able to optimize starting from initial points both close and relatively far from the optimum point.

Significant increases in the mass flow rate are found by optimizing the geometry at a lower Mach number. This also indicates that $25-50\%$ of potential the mass flow rate is lost by using a constant geometry. In other words, there is a significant benefit to changing the shape of the inlet between the two operating conditions. It should also be noted that the more significant increase for the three-dimensional case is partially due to the initial point being further away from the optimum relative to the two-dimensional case. Another interesting result is that the three-dimensional case has achieved greater mass flow per meter span than the two-dimensional case.

Given these results, it is clear that using the adjoint method of calculating the gradient of the mass flow rate is an efficient method to optimize a hypersonic inlet geometry. This method of optimization could

American Institute of Aeronautics and Astronautics
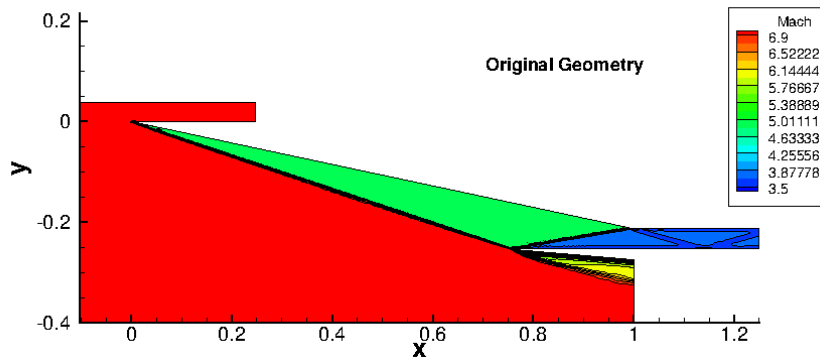
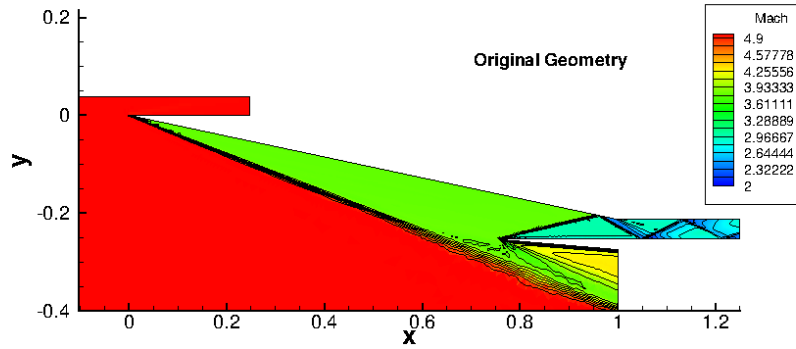(a) Initial geometry at Mach 7.0. $\dot{m} = 18.197 \frac{kg}{s}$ per meter.
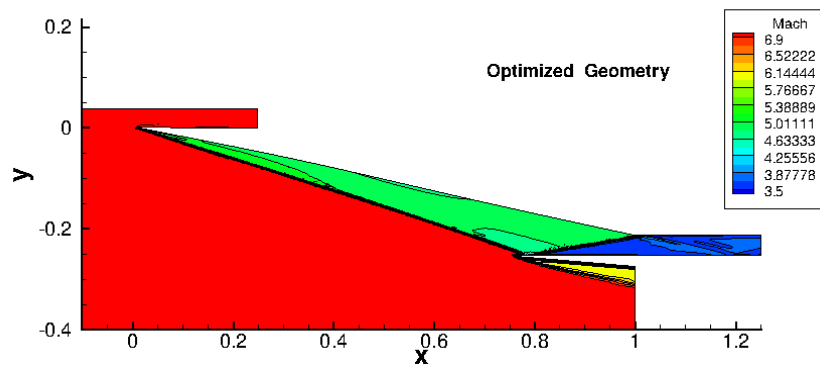
(b) Optimized geometry after 103 function evaluations and 10 optimizer iterations. $\dot{m} = 18.312 \frac{kg}{s}$ per meter.
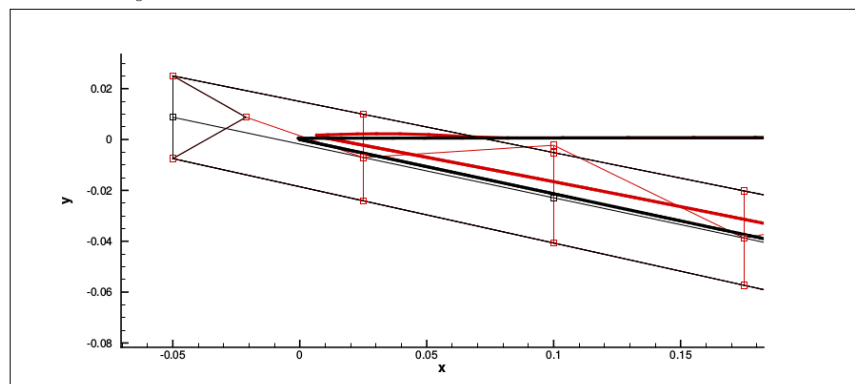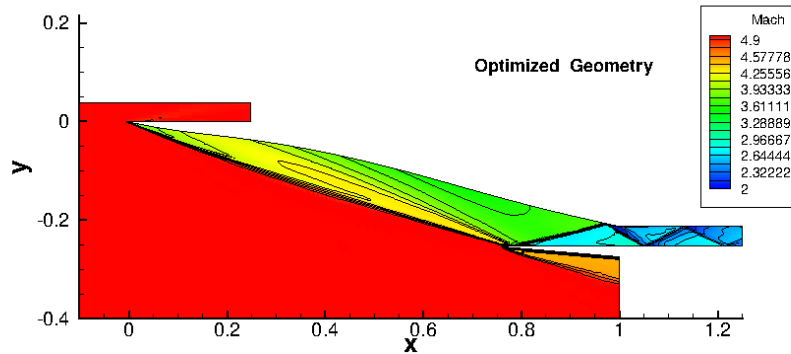

(c) Detail of optimized geometry (red) and original geometry (black) with FFD box control points overlaid.
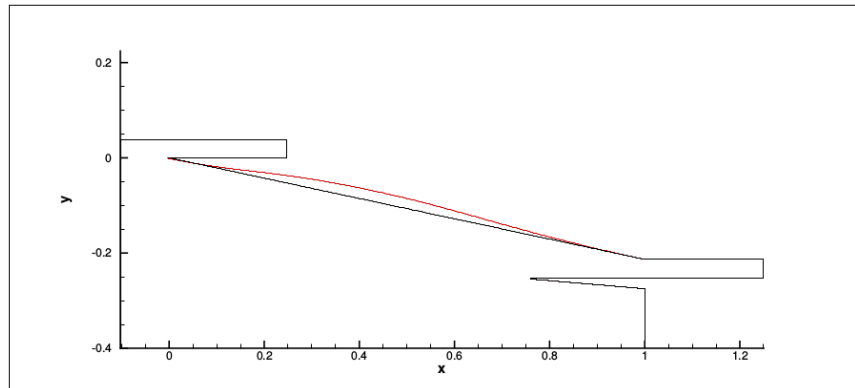
Figure 13: Optimization results at Mach 7.0 with 7 design variables.

American Institute of Aeronautics and Astronautics

(a) Initial geometry at Mach 5.0. $\dot{m} = 10.348 \frac{kg}{s}$ per meter.

(b) Optimized geometry after 90 function evaluations and 10 optimizer iterations. $\dot{m} = 13.012 \frac{kg}{s}$ per meter

(c) Optimized geometry (red) and original geometry (black).

Figure 14: Optimization Results at mach 5.0 With 7 Design Variables.

Eqn.	Geo.	M_0	Initial $\dot{m}$	Final $\dot{m}$	% Δ	Function evaluations.	Design variables
Euler	2D	7	$18.197 \frac{kg}{m\ s}$	$18.312 \frac{kg}{m\ s}$	0.63%	103 CFD, 10 adjoint	7 Design Variables
RANS	2D	7	$17.657 \frac{kg}{m\ s}$	$18.290 \frac{kg}{m\ s}$	3.58%	19 CFD, 6 adjoint	7 Design Variables
Euler	2D	5	$10.348 \frac{kg}{m\ s}$	$13.012 \frac{kg}{m\ s}$	25.78%	90 CFD, 10 adjoint	7 Design Variables
Euler	3D	5	$0.4944 \frac{kg}{s}$	$0.7871 \frac{kg}{s}$	59.20%	55 CFD, 10 adjoint	15 Design Variables

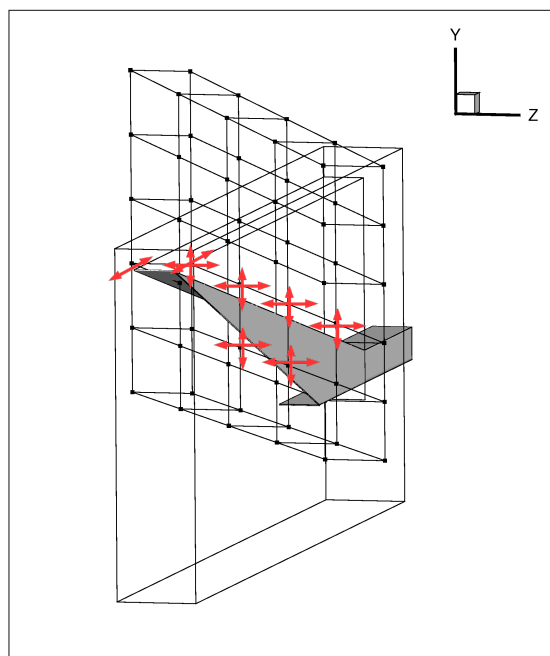Table 1: Summary of optimization results.

Figure 15: FFD box used for 3D inviscid optimization at Mach 5.0. 15 design variables were used, some of which are shown. Vertical deformations along the symmetry plane (not shown) were included as design variables, in addition to the spanwise, horizontal, and vertical deformations shown.

be applied to more complex geometries, for example starting from a REST-class inlet with boundary layer corrections to further improve the design. Other objective functions on outlets can be implemented in the same manner as $\dot{m}$. Using the adjoint method to calculate gradients significantly reduces the computational cost of this optimization, making it more feasible to use multidisciplinary and multi-physics optimization in the future.

Further work in this area could include using different objective or multiple objectives, incorporating other portions of the engine flow path such as the combustor and nozzle, and incorporating aero-thermo-structural effects. The current objective function could also be applied to robust optimization, and other design studies.

VII.   Acknowledgements

References

[1]Hank, J. M., Murphy, J. S., and Mutzman, R. C., "The X-51A Scramjet Engine Flight Demonstration Program," *15th AIAA International Space Planes and Hypersonic Systems and Technologies Conference*, , No. May, April 2008, pp. 1–13.

[2]Marshall, L., Bahm, C., Corpening, G., and Sherrill, R., "Overview With Results and Lessons Learned of the X-43A Mach 10 Flight," *AIAA/CIRA 13th International Space Planes and Hypersonics Systems and Technologies Conference*, May 2005, pp. 1–23.

[3]Jackson, K., Gruber, M., and Barhorst, T., "The HIFiRE flight 2 experiment: an overview and status update," *AIAA Paper*, , No. August, Aug. 2009.

[4]Busemann, A., "Die achsensymmetrische kegelige Überschallströmung," *Luftfahrtforschung*, Vol. 19, No. 4, 1942, pp. 137–144.

[5]Billig, F. S., Baurle, R. A., Tam, C.-J., and Wornom, S. F., "Design and analysis of streamline traced hypersonic inlets," *AIAA paper*, Vol. 4974, 1999, pp. 1999.

[6]Smart, M. K., "Design of Three-Dimensional Hypersonic Inlets with Rectangular-to-Elliptical Shape Transition," *Journal*
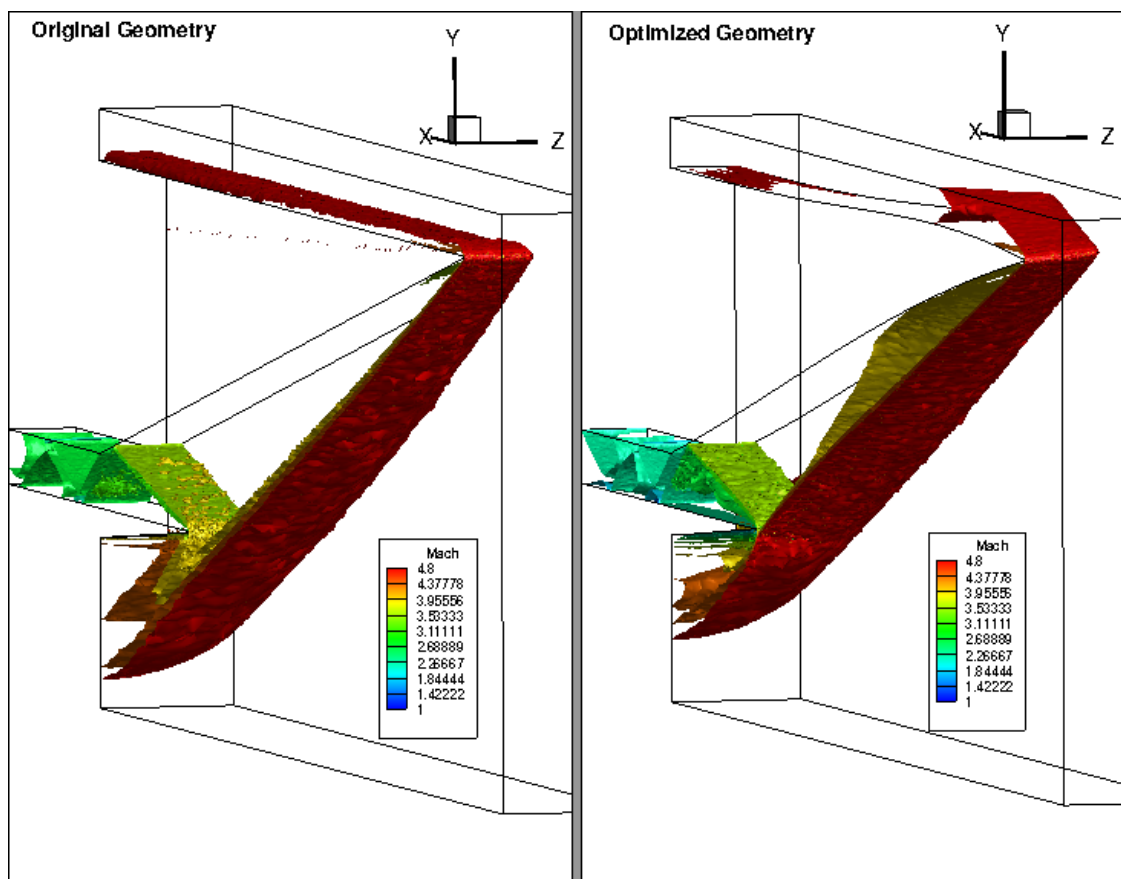
Figure 16: Three dimensional inviscid optimization results at Mach 5.0. Isosurfaces of Mach number indicate that the shock has moved to nearly meet both the cowl lip and the side wall.

of Propulsion and Power, Vol. 15, No. 3, May 1999, pp. 408–416.

[7]Gollan, R. and Ferlemann, P., "Investigation of REST-class Hypersonic Inlet Designs," *17th AIAA International Space Planes and Hypersonic Systems and Technologies Conference*, April 2011.

[8]Tarn, C.-J. and Baurle, R. A., "Inviscid CFD analysis of streamline traced hypersonic inlets at off-design conditions," *39th Aerospace Sciences Meeting and Exhibit, Reno, NV*, 2001.

[9]Jameson, A., "Aerodynamic Design via Control Theory," *Journal of Scientific Computing*, Vol. 3, No. 3, 1988, pp. 233–260.

[10]Wang, Q., Duraisamy, K., Alonso, J. J., and Iaccarino, G., "Risk assessment of scramjet unstart using adjoint-based sampling methods," *AIAA journal*, Vol. 50, No. 3, 2012, pp. 581–592.

[11]Kline, H., Palacios, F., and Alonso, J. J., "Sensitivity of the Performance of a 3-Dimensional Hypersonic Inlet to Shape Deformations," *19th AIAA International Space Planes and Hypersonic Systems and Technologies Conference*, Atlanta, GA, June 2014.

[12]Anderson Jr., J. D., *Hypersonic and High-Temperature Gas Dynamics Second Edition*, AIAA Education Series, AIAA, Blacksburg, Virginia, 2nd ed., 2006.

[13]Smart, M. K., "How Much Compression Should a Scramjet Inlet Do?" *AIAA Journal*, Vol. 50, No. 3, March 2012, pp. 610–619.

[14]Cantwell, B. J., *Aircraft and Rocket Propulsion; Course Reader*, Stanford, CA, 2007.

[15]Hirsch, C., *Numerical Computation of Internal and External Flows*, Vol. 2, John Wiley & Sons, 1990.

[16]Palacios, F., Economon, T. D., Wendorff, A. D., and Alonso, J., "Large-scale aircraft design using SU2," *53st AIAA Aerospace Sciences Meeting*, 2015, pp. 2015–1946.

[17]Giles, M. B. and Pierce, N. A., "Adjoint equations in CFD : duality , boundary conditions and solution behaviour," *AIAA*, 1997.

[18]Castro, C., Lozano, C., Palacios, F., and Zuazua, E., "Systematic Continuous Adjoint Approach to Viscous Aerodynamic Design on Unstructured Grids," *AIAA Journal*, Vol. 45, No. 9, Sept. 2007, pp. 2125–2139.

[19]Hayashi, M., Ceze, M., and Volpe, E., "Characteristics-based boundary conditions for the Euler adjoint problem," *International Journal for Numerical Methods in Fluids*, Vol. 71, No. 10, 2012, pp. 1297–1321.

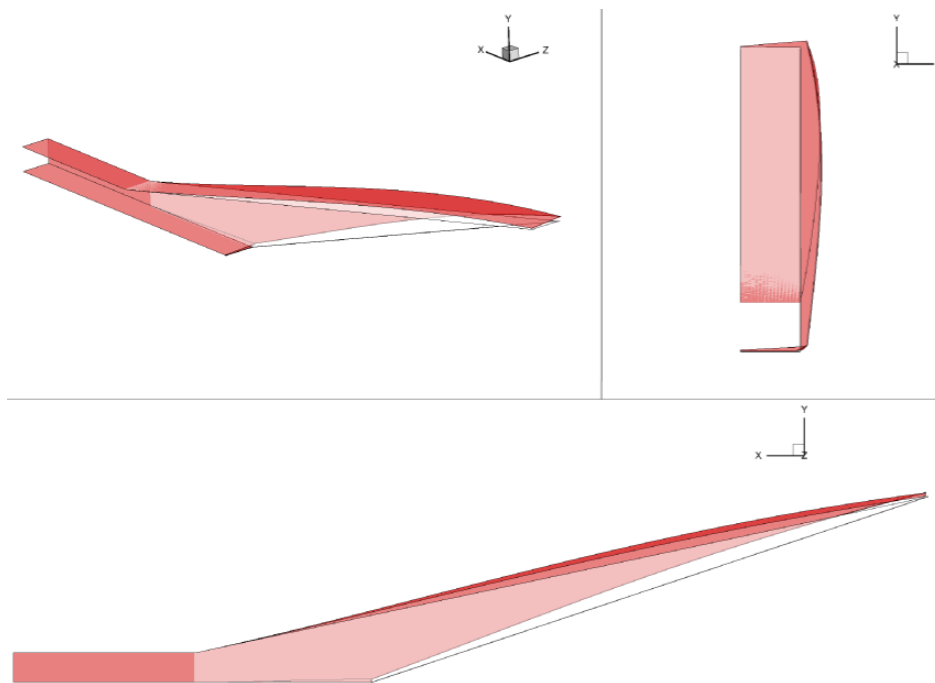American Institute of Aeronautics and Astronautics

Figure 17: Three dimensional inviscid optimization results at Mach 5.0. Red surfaces are optimized design, white surfaces are the original geometry.
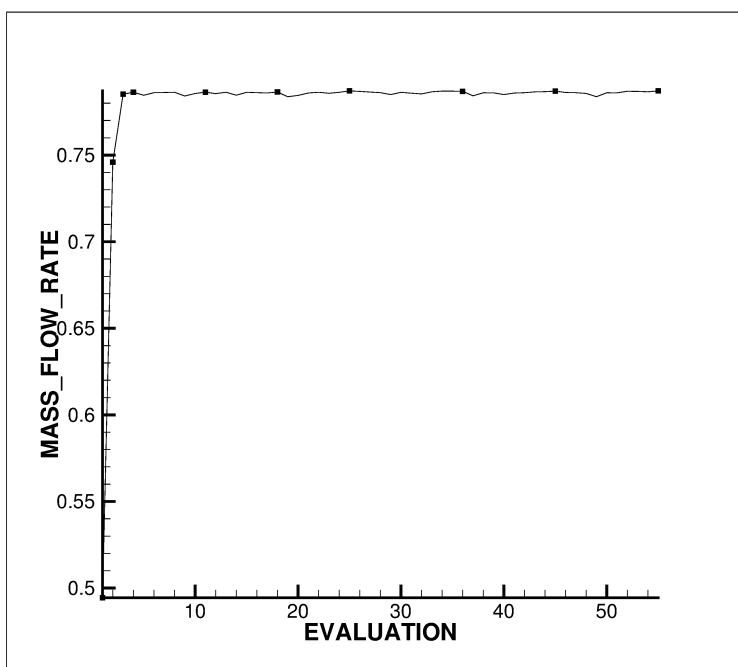

Figure 18: Three dimensional inviscid optimization history at Mach 5. History of evaluations including internal line searches, with the major optimization iterations marked by squares.

[20]Economon, T. D., *Optimal Shape Design Using an Unsteady Continuous Adjoint Approach*, Ph.D. thesis, Department of Aeronautics and Astronautics, Stanford University, 2014.

American Institute of Aeronautics and Astronautics
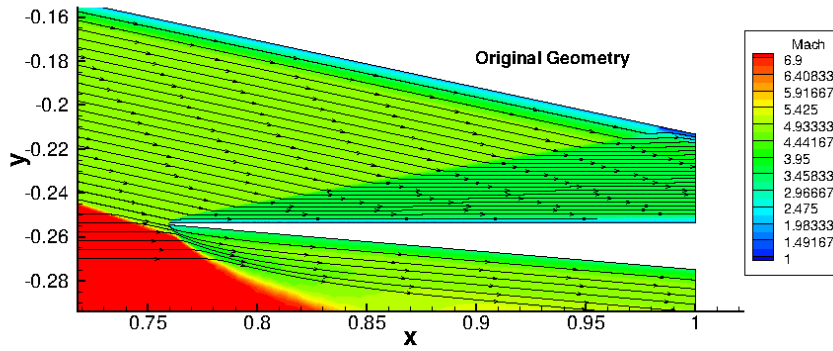
(a) Initial geometry at Mach 7.0, viscous flow. $\dot{m} = 17.658 \frac{kg}{s}$ per meter
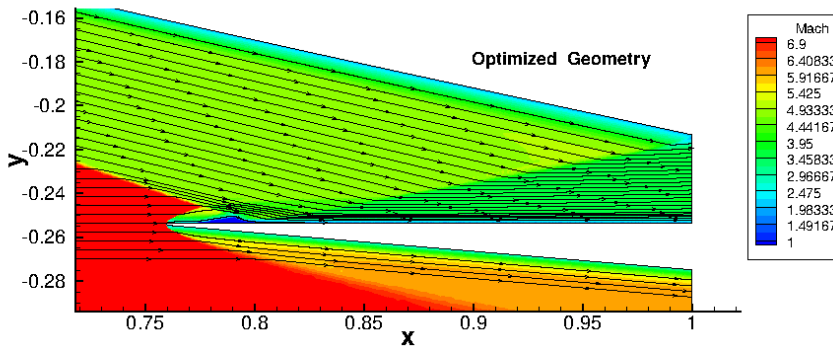
(b) Optimized geometry after 30 function evaluations and 6 optimizer iterations.
$\dot{m} = 18.290 \frac{kg}{s}$ per meter

Figure 19: Optimization results at Mach 7.0 with 7 design variables.

[21]Papadimitriou, D. and Giannakoglou, K., "Total pressure loss minimization in turbomachinery cascades using a new continuous adjoint formulation," *Proceedings of the Institution of Mechanical Engineers, Part A: Journal of Power and Energy*, Vol. 221, No. 6, 2007, pp. 865–872.

[22]Economon, T. D., Palacios, F., and Alonso, J. J., "An Unsteady Continuous Adjoint Approach for Aerodynamic Design on Dynamic Meshes," *AIAA Paper 2014-2300*, 2014.

[23]Palacios, F., Colonno, M., Aranake, A., Campos, A., Copeland, S., Economon, T., Lonkar, A., Lukaczyk, T., Taylor, T., and Alonso, J., "Stanford University Unstructured (SU2): An open-source integrated computational environment for multi-physics simulation and design," *51st AIAA Aerospace Sciences Meeting and Exhibit.*, Grapevine, TX, Jan. 2013.

[24]Samareh, J. A., "Aerodynamic shape optimization based on Free-Form deformation," *AIAA Paper 2004-4630*, 2004.

[25]Kenway, G., Kennedy, G., and Martins, J. R. R. A., "A CAD-Free Approach to High-Fidelity Aerostructural Optimization," *AIAA Paper 2010-9231*, 2010.

[26]Anderson, G., Aftosmis, M., and Nemec, M., "Parametric Deformation of Discrete Geometry for Aerodynamic Shape Design," *AIAA Paper 2012-0965*, 2012.

[27]Python Software Foundation, "Python 2.7.6 Release," https://www.python.org/download/releases/2.7.6/, 2015.

[28]Jameson, A., Schmidt, W., and Turkel, E., "Numerical solution of the Euler equations by finite volume methods using Runge-Kutta time stepping schemes," *AIAA Paper 1981-1259*, 1981.

[29]Turner, J. C. and Smart, M. K., "Application of inlet injection to a three-dimensional scramjet at Mach 8," *AIAA journal*, Vol. 48, No. 4, 2010, pp. 829–838.

VIII.   Appendix: Additional Details

This section contains details of the Jacobian and other terms used in the derivation of the adjoint equations and boundary conditions.

American Institute of Aeronautics and Astronautics

Jacobian matrix for two dimensional Euler Equations.

$$A_x M = \frac{\partial F_x}{\partial U} \frac{\partial U}{\partial V} = \frac{\partial F_x}{\partial V} = \begin{bmatrix} u & u^2 & uv & \frac{1}{2}uv^2 \\ \rho & 2\rho u & \rho v & \rho(H + u^2) \\ 0 & 0 & \rho u & \rho uv \\ 0 & 1 & 0 & \frac{u\gamma}{(\gamma-1)} \end{bmatrix} \quad (18)$$

Transformation between conservative and primitive variables.

$$M = \begin{bmatrix} \frac{\partial U}{\partial \rho} & \frac{\partial U}{\partial \vec{v}} & \frac{\partial U}{\partial \rho} \end{bmatrix} = \begin{bmatrix} 1 & 0 & 0 \\ \vec{v} & \rho \bar{\bar{I}} & 0 \\ \frac{v^2}{2} & \rho \vec{v}^T & \frac{1}{\gamma-1} \end{bmatrix} \quad (19)$$

$$\vec{A} = ((A_x), (A_y), (A_z)) \quad (20)$$

Eigenvalues of the Jacobian for the Euler Equations.

$$\Lambda = \begin{bmatrix} u & 0 & 0 & 0 \\ 0 & u & 0 & 0 \\ 0 & 0 & u-c & 0 \\ 0 & 0 & 0 & u+c \end{bmatrix} \quad (21)$$

Design Parameters	
M_0	7.0
L_1	1.0 meters
P_2/P_0	20
Resulting Dimensions	
L_2	.2398 meters
h_1	.2535 meters
h_2	.0402 meters

Figure 20: Two-dimensional inlet design.

American Institute of Aeronautics and Astronautics
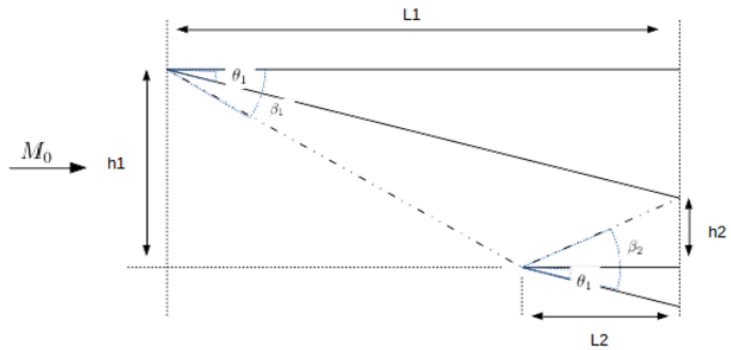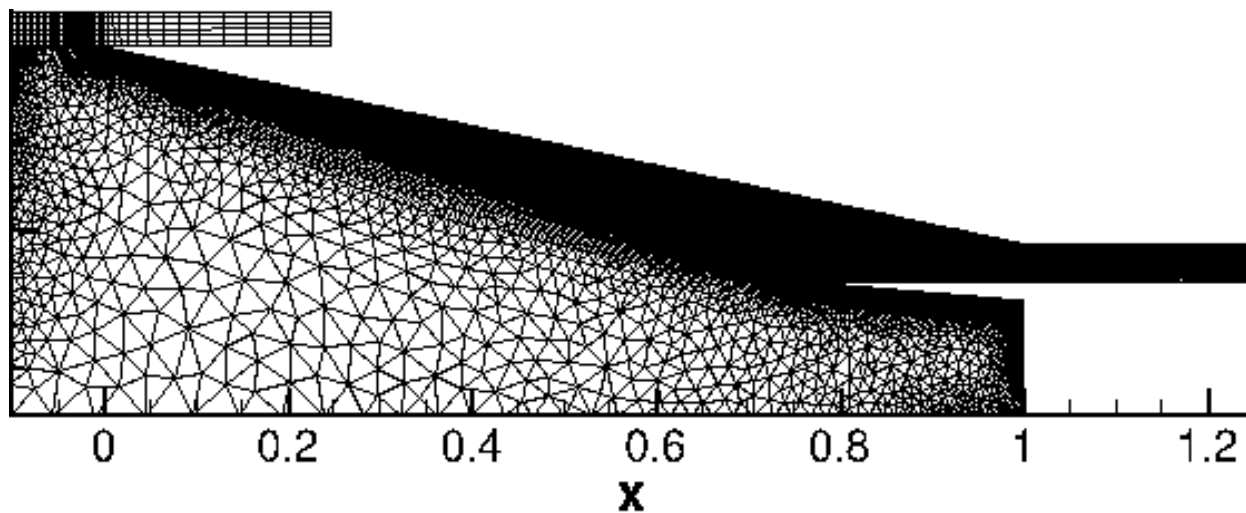
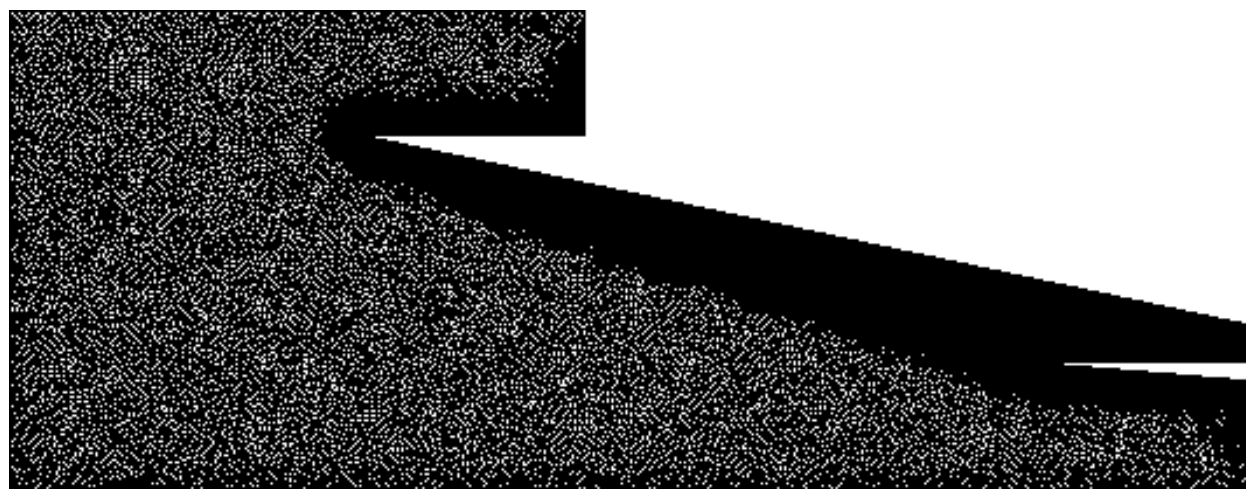Figure 21: Unstructured mesh of 31,330 elements used for two-dimensional inviscid simulations.

Figure 22: Unstructured mesh of 1,120,620 elements used for two-dimensional viscous simulations. Cell spacing near walls such that $y+ \leq 1.0$.

American Institute of Aeronautics and Astronautics